Linear Covariance Analysis of Entry and Aerocapture Trajectories in an Uncertain Atmosphere

Jack Ridderhof* and Panagiotis Tsiotras†
Georgia Institute of Technology, Atlanta, GA, 30332, USA

Samuel W. Albert‡ and Hanspeter Schaub§
University of Colorado Boulder, Boulder, CO, 80303, USA

Planetary entry and aerocapture trajectories are significantly impacted by random variability in atmospheric density. The ability to rapidly quantify the impact of this uncertainty on the vehicle trajectories can improve onboard guidance during atmospheric flight by explicitly considering the probability distribution of future uncertain vehicle states. This paper addresses the problem of uncertainty quantification for entry and aerocapture flight by developing a general theory for linear covariance approximation of nonlinear systems that depend on Gaussian random fields. The Karhunen–Loève expansion is used to parametrically represent the Gaussian random field uncertainty, and then the closed-loop trajectory dispersions are approximated with respect to a given nominal trajectory by a linear covariance method. Numerical examples for guided entry and aerocapture at Mars, with Mars-GRAM generated atmosphere variations, demonstrate a close agreement between the proposed approximation and Monte Carlo.

I. Introduction

HYPERSONIC atmospheric flight, whether with the intent to land on the surface of the planet or skip out of the atmosphere on an aerocapture trajectory, is a challenging domain influenced by a number of significant uncertainties. Most importantly, inherent spatial and temporal variability in atmospheric density must be accounted for at any relevant destination, including Earth. Errors and uncertainties in the actual and navigated state of the vehicle at entry, as well as the aerodynamic properties of the vehicle, play an important role. In order to mitigate these uncertainties and fly a vehicle to a desired final state within small error bounds, some version of closed-loop onboard guidance is required. Even for vehicles that fly open-loop or passively, the distributions of these uncertainties and their impact on key mission parameters must be carefully quantified to ensure the mission requirements are met.

Flight-heritage and current state-of-the-art guidance algorithms generally handle these uncertainties by treating the problem as a deterministic one, then updating commands based on new estimates of the current state. For example, the longitudinal component of the Apollo final phase guidance computes bank angle commands based on current navigated states and the adjoint equations evaluated along a reference trajectory [1]. The Mars Science Laboratory (MSL) mission used a derivative of this approach to guide the entry vehicle during hypersonic flight to follow a provided reference trajectory [2]. A continuing increase in the amount of computing power available onboard has led to a number of numerical predictor-corrector (NPC) approaches, including the Orion entry guidance and state-of-the-art algorithms that have been proposed for both entry and aerocapture [3–5]. While the NPC approach eliminates the need to linearize the dynamics around a reference trajectory, these algorithms still make error predictions and compute corrective commands based on a deterministic prediction of the dynamics. In other words, the structure of all of these guidance schemes implicitly controls uncertainty, and the effectiveness of this approach is estimated in uncertainty quantification studies of the closed-loop dynamics, namely via Monte Carlo analyses.

An alternative guidance approach is to *explicitly* control uncertainty by considering the effect of present and future control decisions on the trajectory uncertainty evolution. While, in general, the complexity of uncertainty quantification

*PhD student, Daniel Guggenheim School of Aerospace Engineering, 270 Ferst Dr., Atlanta, GA 30332.

†David and Andrew Lewis Chair Professor, Daniel Guggenheim School of Aerospace Engineering, and Institute for Robotics and Intelligent Machines, 270 Ferst Dr., Atlanta, GA 30332. AIAA and AAS Fellow.

‡PhD Student, Ann and H.J. Smead Aerospace Engineering Sciences, 3775 Discovery Drive, 429 UCB – CCAR, Boulder, CO 80303. AIAA Student Member.

§Glenn L. Murphy Chair of Engineering, Ann and H.J. Smead Aerospace Engineering Sciences, 3775 Discovery Drive, 429 UCB – CCAR, Boulder, CO 80303. AIAA and AAS Fellow.

prohibits optimization with respect to uncertainties, for many applications treating only the mean and covariance of a linearized system provides a useful and representative surrogate for the true state uncertainty; this approach is referred to as linear covariance analysis [6]. Rapid approximate uncertainty quantification, via linear covariance analysis, can be a useful tool for mission design when used in conjunction with Monte Carlo methods. Furthermore, the effect of feedback control for linearized system models is well understood, and thus linearization methods present an avenue to include stochasticicty and closed-loop system behavior for guidance optimization [7, 8], including possible onboard optimization.

Recent developments in stochastic optimal control further motivate the study of linear stochastic systems. Assuming a control law to be the sum of a nominal input and a linear feedback term, the mean state trajectory is controlled by the nominal control, while the state covariance is steered by the feedback gain. Thus, the terms in the control law appear as the inputs steering the state probability distribution. If a linear stochastic system is controllable, then the selection of a time-varying state feedback gain can lead the state to be distributed with any desired positive-definite covariance in finite time [9, 10]. Constraints on the probability distribution of an uncertain state, which are referred to as chance constraints, introduce a coupling between the planned nominal control inputs and the uncertain corrective closed-loop control inputs [11]. Chance constraints on linear Gaussian-distributed systems can be formulated as convex constraints on the nominal control and the feedback gain [12]; nonlinear systems can be similarly treated via successive convexification [11]. It follows that, via the application of chance constraints, stochastic methods allow for a measured trade-off between performance margin and nominal performance since the state and control probability distributions are included in the optimization [13].

To be incorporated into the linear covariance analysis as a parameter subject to perturbations, density variability must be explicitly expressed in some analytical form. Thus, generating dispersed profiles of atmospheric density from some semi-empirical model, as is commonly done for Monte Carlo analyses [14, 15], does not work well. When non-Monte Carlo uncertainty quantification methods are applied to planetary entry and aerocapture, one common approach is to assume an exponential model of density, then simply disperse the surface density and atmospheric scale height [16–18]. However, this is a significant assumption that forgoes a higher-fidelity approach to modeling density variability. As an intermediate approach, recent work has shown that density variability at Mars as modeled by the Mars Global Reference Atmospheric Model (Mars-GRAM 2010) is well-approximated by a Gaussian random field, and can thus be represented in terms of a Karhunen–Loève expansion [19, 20]. This provides an analytical form of density perturbations that can be incorporated into a linear covariance analysis while allowing for a higher-fidelity model of density variability.

In this paper, atmospheric density is modeled as a Gaussian random field and subsequently approximated parametrically via Karhunen–Loève expansion. A linear covariance model is constructed with respect to the Karhunen–Loève expansion terms of the density model, and the approximate trajectory covariance evolution is computed via numerical integration of the matrix-valued linear system. The approximate covariance evolution along a hypersonic vehicle trajectory as computed by the proposed method is compared to Monte Carlo for entry and aerocapture scenarios at Mars using Mars-GRAM to model density variation.

II. Linear Covariance Analysis in Gaussian Random Fields

The domain of linear analysis follows from the basic principle that a large class of functions may be reasonably approximated to first order. That is, for a smooth mapping $f : x \mapsto y$, the difference of the output y from a nominal output $\bar{y} = f(\bar{x})$ can be reasonably approximated as

$$y - \bar{y} \approx F(x - \bar{x}), \quad \text{where} \quad F = \frac{\partial f}{\partial x}(\bar{x}). \tag{1}$$

Furthermore, in the case where the input x is a Gaussian distributed random vector with mean $\bar{x}$ and covariance X, then the output y can be approximated as a Gaussian random vector with mean $\bar{y} \approx f(\bar{x})$ and covariance

$$Y \approx FXF^{\mathsf{T}}. \tag{2}$$

In the following section, the basic theory of linear covariance analysis is reviewed for dynamical systems, for which the input and output belong to function spaces and the mapping is defined by an ordinary differential equation.

A. Linear Covariance Analysis for Dynamical Systems

Consider a nonlinear dynamical system with state $x \in \mathbb{R}^n$ acting under the influence of q uncertain parameters $p_0 \in \mathbb{R}^q$ according to the dynamics

$$\dot{x} = f(t, x, u(t,x), p_0) = f_{\text{cl}}(t, x, p_0), \quad x(t_0) = x_0, \tag{3}$$

where $u(t,x)$ is a closed-loop control. For generality, let the initial state x_0 be included as an uncertain parameter and define the new $\ell = n + q$ dimensional parameter vector p as the concatenation

$$p = \begin{bmatrix} x_0 \\ p_0 \end{bmatrix} \in \mathbb{R}^\ell. \tag{4}$$

The following analysis, which is adapted from Ref. [21] Ch. 3, is concerned with approximating variations in trajectories of the system (3) as linear functions of variations of the parameter vector p.

Let $x(t,p)$ be the solution to (3) for a particular realization of the parameter vector p, which is given as

$$x(t,p) = x_0 + \int_{t_0}^{t} f_{\text{cl}}\big(\tau, x(\tau,p), p_0\big)\, \mathrm{d}\tau. \tag{5}$$

Taking the partial derivative of the trajectory $x(t,p)$ with respect to the parameter p, we obtain

$$\frac{\partial x}{\partial p}(t,p) = \begin{bmatrix} I_n & 0_{n\times q} \end{bmatrix} + \int_{t_0}^{t} \left\{ \frac{\partial f_{\text{cl}}}{\partial x}\big(\tau, x(\tau,p), p_0\big) \frac{\partial x}{\partial p}(\tau,p) + \frac{\partial f_{\text{cl}}}{\partial p}\big(\tau, x(\tau,p), p_0\big) \right\} \mathrm{d}\tau. \tag{6}$$

Next, we approximate the expression (6) about a given nominal parameter value $\bar{p} = (\bar{x}_0, \bar{p}_0)$. Define the matrix-valued functions of time

$$S(t) = \frac{\partial x}{\partial p}(t, \bar{p}), \quad A_{\text{cl}}(t) = \frac{\partial f_{\text{cl}}}{\partial x}\big(t, x(t,\bar{p}), \bar{p}_0\big), \quad C(t) = \frac{\partial f_{\text{cl}}}{\partial p}\big(t, x(t,\bar{p}), \bar{p}_0\big) = \begin{bmatrix} 0_n & \dfrac{\partial f_{\text{cl}}}{\partial p_0}\big(t, x(t,\bar{p}), \bar{p}_0\big) \end{bmatrix}. \tag{7}$$

The matrix $S(t)$ is known as the *sensitivity function*, since the trajectory $x(t,p)$ can be approximated to first order as

$$x(t,p) \approx x(t,\bar{p}) + S(t)(p - \bar{p}). \tag{8}$$

Furthermore, from (6), the sensitivity function is obtained as the solution to the ODE

$$\dot{S}(t) = A_{\text{cl}}(t) S(t) + C(t), \quad S(t_0) = \begin{bmatrix} I_n & 0_{n\times q} \end{bmatrix}. \tag{9}$$

Now suppose that the parameter vector p_0 is Gaussian distributed as $p_0 \sim \mathcal{N}(\bar{p}_0, P_0)$. If the initial state x_0 is uncorrelated with the parameters p_0 and is also Gaussian distributed with covariance matrix X_0, then the parameter p is also Gaussian distributed as

$$p \sim \mathcal{N}(\bar{p}, P), \quad \text{where} \quad \bar{p} = \begin{bmatrix} \bar{p}_0 \\ \bar{x}_0 \end{bmatrix}, \quad P = \begin{bmatrix} X_0 & \\ & P_0 \end{bmatrix}, \tag{10}$$

It then follows from the sensitivity equation (8) that the state $x(t,p)$ is approximately Gaussian distributed with mean $\bar{x}(t) = x(t,\bar{p})$ and covariance

$$X(t) = S(t) P S^{\mathsf{T}}(t). \tag{11}$$

In summary, the state distribution can be approximated to first order about a nominal trajectory $\bar{x}(t)$ by the following procedure: Integrate the nominal trajectory $\bar{x}(t)$ from (3) with $p_0 = \bar{p}_0$; compute the matrices $A_{\text{cl}}(t)$ and $C(t)$ as functions of $\bar{x}(t)$ as in (7); integrate the matrix-valued ODE (9); and, finally, compute the state covariance from (11).

B. Including Spatially-Dependent Uncertainty

The theory of linear covariance analysis is both well known and widely applied in engineering and aerospace applications [6, 22]. However, many common sources of uncertainty arise as spatially or state-dependent, such as variations in atmospheres, currents, or gravitation. In the following, an eigenbasis decomposition is used to parametrically approximate spatially defined random processes so that spatial uncertainty may be incorporated into linear covariance analysis.

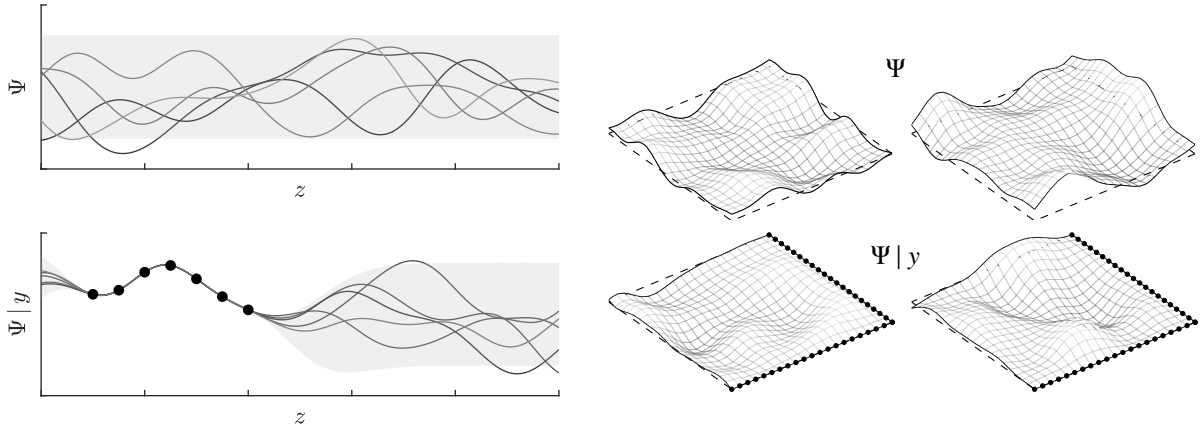

(a) Single-dimensional GRF Ψ conditioned on measurements

(b) Two-dimensional GRF Ψ conditioned to have the rightmost edges be constant

Fig. 1 Samples from one and two-dimensional GRFs

1. Gaussian Random Fields

A collection of random variables $\{\Psi(z) : z \in \mathcal{I} \subseteq \mathbb{R}^d\}$ is a *Gaussian random field* (GRF), also referred to as a Gaussian process, if for any finite set $\{z_i\}_{i=1}^r \subset \mathcal{I}$ the values $\{\Psi(z_i)\}_{i=1}^r$ are *jointly Gaussian* [23, 24]. That is, the value of the field $\Psi(z)$ at any point z in the domain $\mathcal{I}$ is Gaussian distributed, and, furthermore, the values of the field at multiple points form a Gaussian random vector. The collection $\{\Psi(z) : z \in \mathcal{I}\}$ will be simply referred to as as Ψ when the context is clear. A useful property is that a GRFs is fully characterized by a mean function

$$\mu : \mathcal{I} \to \mathbb{R}, \quad \mu(z) = \mathbb{E}\left(\Psi(z)\right), \tag{12}$$

and a positive semi-definite covariance function

$$\Sigma : \mathcal{I} \times \mathcal{I} \to \mathbb{R}, \quad \Sigma(z_1, z_2) = \mathrm{Cov}\left(\Psi(z_1), \Psi(z_2)\right). \tag{13}$$

Thus, the values of the field $\boldsymbol{\Psi} = \left(\Psi(z_1), \ldots, \Psi(z_n)\right)$ at any n input points $\{z_1, \ldots, z_n\} \subset \mathcal{I}$ are Gaussian distributed as $\boldsymbol{\Psi} \sim \mathcal{N}(\boldsymbol{\mu}, \boldsymbol{\Sigma})$, where

$$\boldsymbol{\mu} = \begin{bmatrix} \mu(z_1) \\ \vdots \\ \mu(z_n) \end{bmatrix}, \qquad \boldsymbol{\Sigma} = \begin{bmatrix} \Sigma(z_1, z_1) & \cdots & \Sigma(z_1, z_n) \\ \vdots & \ddots & \vdots \\ \Sigma(z_n, z_1) & \cdots & \Sigma(z_n, z_n) \end{bmatrix}. \tag{14}$$

GRFs are often used in the context of conditioning based on noisy measurements. For example, one- and two-dimensional GRFs, with and without conditioning on measurements, are shown in Figures 1a and 1b. In this paper, however, only the jointly Gaussian property of GRF samples will be used. The interested reader is referred to Ref. [24] for more details on GRFs.

2. Karhunen–Loève Decomposition

While random processes and random fields are infinite dimensional objects, it is possible to obtain a lower-dimensional approximation by projecting onto a set of orthogonal basis functions (a generalized Fourier expansion) [25]. The following result describes an eigenfunction decomposition for GRFs.

Theorem II.1 (Karhunen–Loève (Ref. [26] Thm 6.13.1))**.** *Assume that the domain $\mathcal{I}$ of Ψ is bounded and that the covariance function Σ is continuous and bounded. Then the GRF Ψ may be written as*

$$\Psi(z) = \mu(z) + \sum_{i=1}^{\infty} w_i \varphi_i(z), \tag{15}$$

where $\{\varphi_i\}_{i=1}^{\infty}$ is an orthonormal basis of $L_2(\mathcal{F})$ obtained as the eigenfunctions of the integral operator

$$(T\phi)(z) = \int_{\mathcal{F}} \Sigma(z, z_1)\phi(z_1)\mathrm{d}z. \tag{16}$$

The series in (15) converges in the mean-square sense, that is, for all $z \in \mathcal{F}$,

$$\mathbb{E}\left(\left|\Psi(z) - \sum_{i=1}^{r} w_i\varphi_i(z)\right|^2\right) \to 0, \tag{17}$$

as $r \to \infty$. The random variables $\{w_i\}_{i=1}^{\infty}$ are obtained by

$$w_i = \int_{\mathcal{F}} \Psi(z)\varphi(z)_i\mathrm{d}z, \tag{18}$$

and are Gaussian distributed with zero mean, $\mathbb{E}(w_i) = 0$, and covariance $\mathbb{E}(w_i w_k) = \delta_{i,k}\lambda_i$, where λ_i is the eigenvector of (16) corresponding to the eigenfunction φ_i.

Remark II.2. *The version of the Karhunen–Loève (KL) theorem given as Theorem II.1 is a special case for GRFs. For a general random process the coefficients w_i are mutually independent, but are not necessarily Gaussian distributed. See Refs. [27, 28] for more details on KL for GRFs.*

The eigenbasis decomposition in (15) is useful in that it minimizes the residual mean-square error of any finite truncation of the series (15), provided the terms are properly ordered with decreasing eigenvalues. Indeed, let $\{\eta_i\}_{i=1}^{\infty}$ be an arbitrary orthonormal basis $L_2(\mathcal{F})$, and let ζ_r and ν_r be mean-square error residuals for the r-term expansions as

$$\zeta_r^2 = \mathbb{E}\left(\left|\Psi(z) - \sum_{i=1}^{r} w_i\varphi_i(z)\right|^2\right), \qquad \nu_r^2 = \mathbb{E}\left(\left|\Psi(z) - \sum_{i=1}^{r} q_i\eta_i(z)\right|^2\right), \tag{19}$$

where the random variables q_i are obtained as (18) with the corresponding basis functions q_i. Then $\zeta_r \leq \nu_r$ for all $r \geq 1$ [28].

3. Linear Covariance with Karhunen–Loève Expansions

Consider now a dynamical system that depends on the GRF Ψ, given by

$$\dot{x} = f_\Psi\big(t, x, \Psi(z(x))\big), \quad x(t_0) = x_0, \tag{20}$$

where the argument z of the field Ψ depends on the state x. Replacing Ψ in the system (20) with a q-term truncation

$$\Psi(z) \approx \Psi_q(z) = \mu(z) + \sum_{i=1}^{q} w_i\varphi_i(z), \tag{21}$$

enables an analysis of the random field dependent dynamical system (20) using the linear covariance analysis developed in Subsection II.A. Indeed, after substituting the truncated series (21) into the dynamics (20), the system (20) can be written in the form of the system (3) as

$$\dot{x} = f_\Psi(t, x, \Psi(z(x))) \approx f_\Psi(t, x, \Psi_q(z(x))) = f_{\mathrm{cl}}(t, x, p_0), \tag{22}$$

where $p_0 = (w_1, \ldots, w_q)$ are the coefficients obtained from (18), which have zero mean and covariance

$$P_0 = \begin{bmatrix} \lambda_1 & & \\ & \ddots & \\ & & \lambda_q \end{bmatrix}, \tag{23}$$

where λ_i are the eigenvalues corresponding to the eigenfunctions φ_i. It follows that the partial derivatives of the system (3) as given in (7) depend on the basis functions φ_i by

$$\frac{\partial f_{\mathrm{cl}}}{\partial p_0} = \frac{\partial f_\Psi}{\partial \Psi_q}\frac{\partial \Psi_q}{\partial p_0}, \tag{24}$$

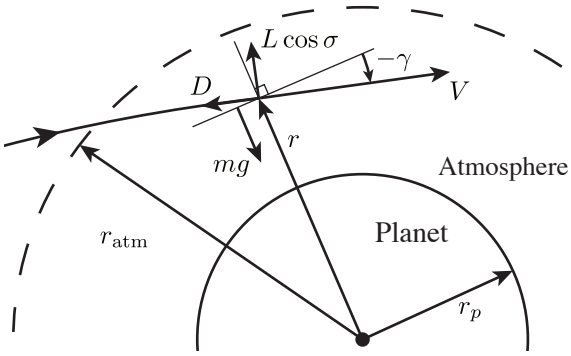

Fig. 2 Longitudinal vehicle coordinates

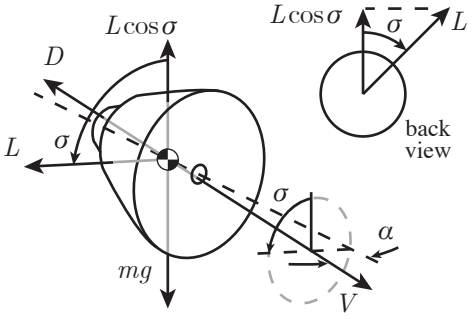

Fig. 3 Bank angle control

where the partials

$$\frac{\partial \Psi_q(z)}{\partial p_0} = \begin{bmatrix} \dfrac{\partial \Psi_q(z)}{\partial w_1} & \cdots & \dfrac{\partial \Psi_q(z)}{\partial w_q} \end{bmatrix} \quad \text{and} \quad \frac{\partial \Psi_q(z)}{\partial w_i} = \varphi_i(z), \tag{25}$$

are evaluated at the nominal values $z = z(\bar{x}(t))$. Note that the nominal trajectory $\bar{x}(t) = x(t, \bar{p})$ is evaluated along the mean value μ of the field Ψ since the nominal value of the parameter p_0 is zero, and the truncation (21) only factors into the linear covariance approximation via the C matrix in (7).

C. Summary

The linear covariance method developed in this section is summarized in the procedure below.

Linear Covariance Approximation with Gaussian Random Fields:

1) Compute a q-term decomposition of Ψ by solving for the eigenvalues and eigenfunctions of (16).
2) Obtain a nominal trajectory $\bar{x}(t)$ for $t \in [t_0, t_f]$.
3) Compute the matrices $A(t)$, $B(t)$, and $C(t)$ as in (7).
4) Integrate the sensitivity equation (9) from t_0 to t_f.
5) Obtain state covariance $X(t)$ from (11).

III. Atmospheric Flight in a Gaussian Random Field

The longitudinal (in-plane) motion of an entry vehicle in atmospheric flight around a spherical, non-rotating planet is described in planet-relative coordinates by the system of equations

$$\dot{r} = V \sin\gamma, \tag{26a}$$

$$\dot{V} = -\frac{\rho V^2}{2\beta} - \frac{\mu_{\text{grav}} \sin\gamma}{r^2}, \tag{26b}$$

$$\dot{\gamma} = \frac{\rho V E}{2\beta}\cos\sigma - \left(\frac{\mu_{\text{grav}}}{r^2} - \frac{V^2}{r}\right)\frac{\cos\gamma}{V}, \tag{26c}$$

$$\dot{R} = V\cos\gamma, \tag{26d}$$

where r is the vehicle radius, V is the planet-relative velocity, γ is the planet-relative flight path angle (FPA), and R is the range traveled [29]. The bank angle σ is the angle between the lift vector and the local vertical, measured about the velocity vector, ρ is atmospheric density, $E = C_L/C_D$ is the lift-to-drag ratio, and $\beta = m/SC_D$ is the spacecraft ballistic coefficient in terms of mass m, reference area S, and drag coefficient C_D. The longitudinal flight coordinates and bank angle definition are shown in Figures 2 and 3.

The density ρ, which depends on the altitude h, is a random process, and thus is a challenging aspect of controlling and modeling uncertainty for vehicles in atmospheric flight. In the following sections, the theory developed in Section II is applied to solve the problem of uncertainty quantification with an random density process.

A. Representing Uncertainty

The density uncertainty is assumed to follow the model internal to Mars-GRAM 2010 [30]. Samples of density as a function of altitude

$$\boldsymbol{\rho} = \begin{bmatrix} \rho(h_1) & \cdots & \rho(h_{N_h}) \end{bmatrix}^\intercal, \tag{27}$$

for a given grid of input altitudes $\{h_i\}_{i=1}^{N_h}$, are generated by Mars-GRAM 2010. The density function $\rho(h)$ is then log-linearly interpolated from the samples in (27). Recent studies by the authors have suggested that Mars-GRAM is well approximated as a GRF [7, 8, 20], and thus can be represented by a KL decomposition as

$$\rho(h) \approx \bar{\rho}(h) + \sum_{i=1}^{q} w_i \varphi_i(h), \tag{28}$$

where $\bar{\rho}(h)$ is the mean density profile. Since the density process is defined by discrete points sampled from Mars-GRAM, the eigenvalues and eigenfunctions of the covariance operator (16) are computed numerically from the sample covariance.

The built-in Monte Carlo functionality of Mars-GRAM 2010 is used to compute N_s samples $\{\boldsymbol{\rho}_i\}_{i=1}^{N_s}$ of the density as in (27) at the discrete altitude values $\{h_i\}_{i=1}^{N_h}$. The mean density $\bar{\rho}(h)$ is a log-linear interpolation of the sample mean of $\{\boldsymbol{\rho}_i\}_{i=1}^{N_s}$, and the covariance operator equation (16) is approximated by the sample covariance as follows. Let $\boldsymbol{\Sigma}$ be the sample covariance matrix defined as

$$\boldsymbol{\Sigma} = \frac{1}{N_s + 1} \Gamma \Gamma^\intercal, \qquad \text{where} \qquad \Gamma = \begin{bmatrix} \boldsymbol{\rho}_1 & \cdots & \boldsymbol{\rho}_{N_s} \end{bmatrix}. \tag{29}$$

An approximation of the eigenfunctions $\varphi_i(h)$ and eigenvalues λ_i are is obtained by solving the matrix eigenvalue problem

$$\boldsymbol{\Sigma}\boldsymbol{\varphi}_i = \lambda_i \boldsymbol{\varphi}_i, \qquad \text{where} \qquad \boldsymbol{\varphi}_i = \begin{bmatrix} \varphi_i(h_1) & \cdots & \varphi_i(h_{N_h}) \end{bmatrix}^\intercal. \tag{30}$$

The functions $\varphi_i(h)$ are approximated by linearly interpolating the vectors $\boldsymbol{\varphi}_i$.

It follows that any realization of the q-dimensional approximation of the density (28) is obtained by sampling the q Gaussian random variables $\{w_i\}_{i=1}^{q}$. This empirical version of a KL expansion is sometimes referred to by other terms including Karhunen–Loève transform. The resulting profiles of density variation $\delta\rho = \rho/\bar{\rho} - 1$ obtained from the KL expansion model are compared with profiles from Mars-GRAM in Figure 4. Note that since the nominal density is exponential, the absolute effect of density variation is much larger at lower altitudes, and thus the first terms of the KL expansion capture density variations at lower altitudes.

1. Notes on implementation

In practice, there is more than one correct way to construct a KL expansion to represent density. The above derivation assumes an expansion on the value of density itself; however, because density varies by orders of magnitude over the relevant altitudes, it can sometimes be beneficial to instead expand the normalized perturbation of density $\delta\rho$, which is defined by

$$\delta\rho = \rho/\bar{\rho} - 1. \tag{31}$$

To construct a KL expansion for $\delta\rho$, simply apply (31) to the density sample data (using the sample mean to approximate $\bar{\rho}$), follow the normal steps to define the KL expansion, and then when evaluating the approximation recover density as $\rho(h_i) = (\delta\rho(h_i) + 1)\bar{\rho}(h_i)$. Other normalization factors could also be chosen, such as the dynamic pressure along the reference trajectory at that altitude, noting that this particular example would be a poor choice if altitude is not monotonically decreasing along the reference trajectory as is the case for aerocapture or lofted entries.

In this work the number of terms included in the KL summation was simply set to $q = 50$, which was observed to perform well in this approximation. Alternatively, it is also possible to select the value of q based on a desired threshold for the mean-square error. For some level of permissible relative mean-square norms error $(1 - \alpha) \times 100\%$ and some sufficiently large number of terms k, one heuristic for selecting q is as follows:

$$q = \min \left\{ j : \frac{\sum_{i=1}^{j} \lambda_i}{\sum_{i=1}^{j+k} \lambda_i} \geq \alpha \right\}. \tag{32}$$

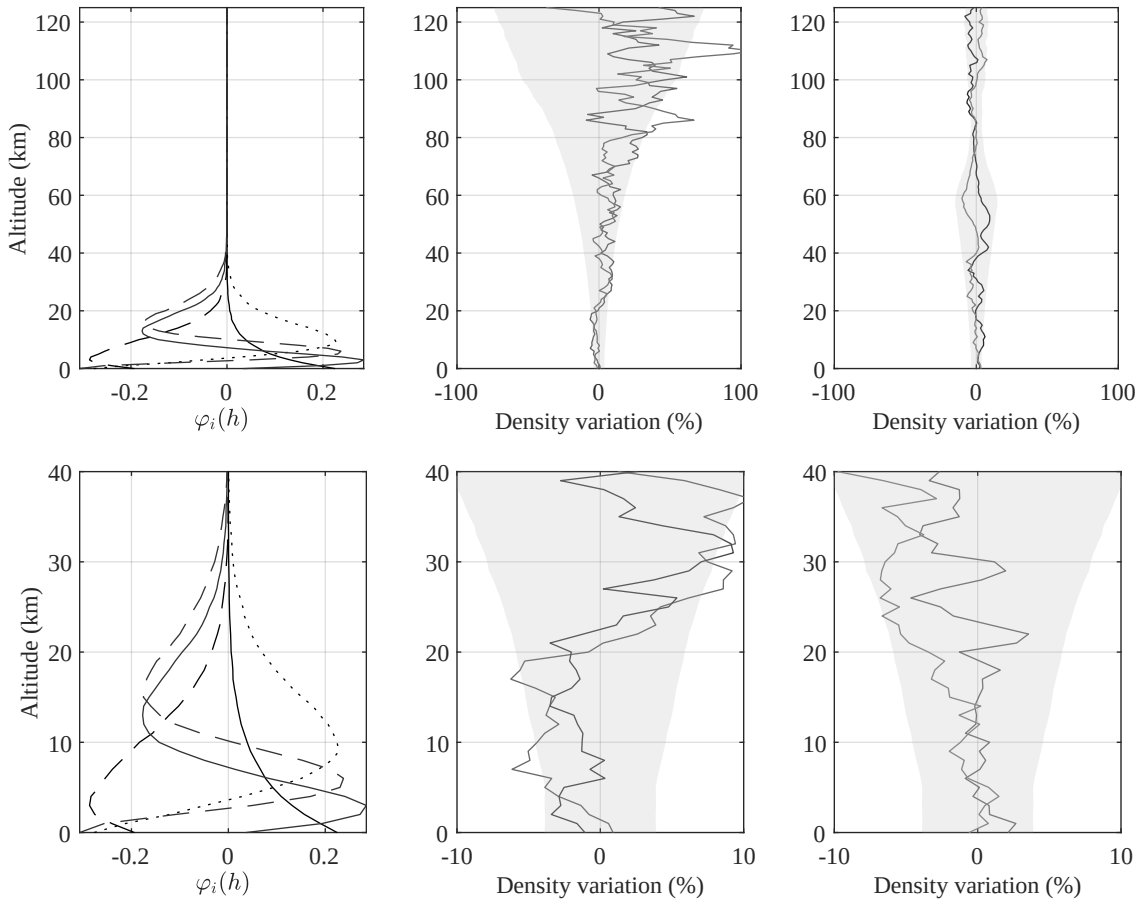

Fig. 4 Left: First five basis functions from (30). Middle: Mars-Gram samples. Right: 40-term KL samples. On the middle and right plots, two samples are shown over a shaded region denoting the 2σ confidence interval.

B. Linear Sensitivity

In order to compute the sensitivity matrix and perform linear covariance analysis for the closed-loop dynamical system, the matrices $A_{cl}(t)$ and $C(t)$ must be derived according to (7). The control input u, which is taken to be the cosine of the bank angle $u = \cos\sigma$, is assumed to follow the linear feedback law

$$u(t,x) = \bar{u}(t) + K(t)\big(x - \bar{x}(t)\big), \tag{33}$$

for a given feedback gain matrix $K(t)$. The closed-loop matrix $A_{cl}(t)$ can then be expressed as

$$A_{\mathrm{cl}}(t) = \frac{\partial f_{\mathrm{cl}}}{\partial x} = \frac{\partial f}{\partial x} + \frac{\partial f}{\partial u}\frac{\partial u}{\partial x} = A(t) + B(t)K(t), \tag{34}$$

where the matrices $A(t)$ and $B(t)$ are evaluated along the reference trajectory $\bar{x}(t)$ and $\bar{u}(t)$. The matrices $A(t)$, $B(t)$, and $C(t)$ are provided for this dynamical system in Appendix A.

IV. Numerical Examples

A. Guided Mars Entry

1. Problem Definition

Consider a Mars Science Laboratory (MSL)-like vehicle performing a guided entry at Mars. The vehicle lift-to-drag ratio is $E = 0.24$, the ballistic coefficient is $\beta = 130$ kg/m^2, and Mars is assumed to have gravitational parameter

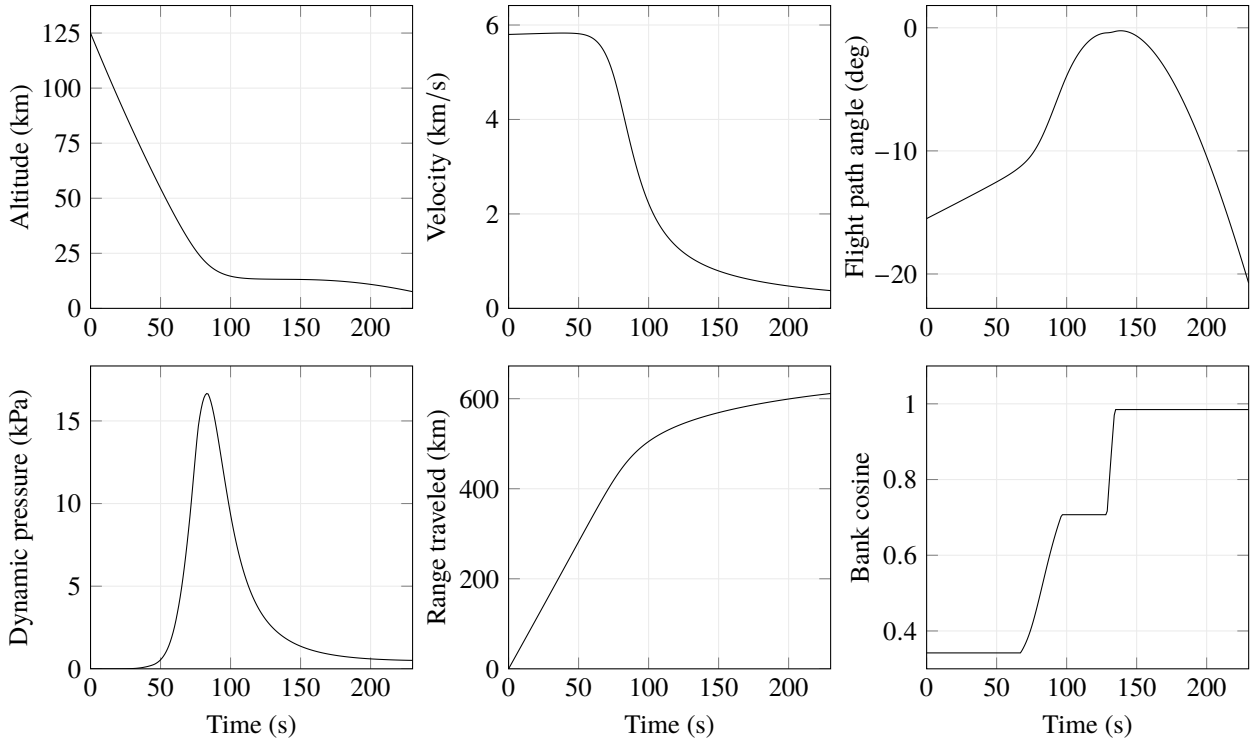

Fig. 5 Nominal entry trajectory

Table 1 Vehicle and planetary parameters for entry and aerocapture examples

Parameter	Value
Lift-to-Drag ratio, E	0.24
Ballistic Coefficient, β	130 kg/m^2
Gravitational Parameter, μ_{grav}	4.2828×10^{13} m^3/s^2
Surface Radius, r_p	3397 km

$\mu_{\text{grav}} = 4.2828 \times 10^{13}$ m^3/s^2 and surface radius $r_p = 3397$ km; these parameters are listed in Table 1. At the initial time $t_0 = 0$ the vehicle is nominally at an altitude of 125 km with planet-relative velocity 5.8 km/s and flight path angle $-15.5°$. The vehicle state error from these nominal values is Gaussian distributed such that the 3σ errors of velocity, flight path angle, and downrange distance are 20 m/s, 0.5°, and 5 km, respectively; the initial altitude is assumed to be exactly 125 km, by definition of the initialization condition at entry interface. Thus the initial state is Gaussian distributed as

$$x_0 \sim \mathcal{N}(\bar{x}_0, P_0), \quad \text{where} \quad \bar{x}_0 = \begin{bmatrix} 125\,\text{km} + r_p \\ 5.8\,\text{km/s} \\ -15.5° \\ 0 \end{bmatrix}, \quad P_0 = \begin{bmatrix} 0 & & & \\ & (20\,\text{m/s}/3)^2 & & \\ & & (0.5°/3)^2 & \\ & & & (5\,\text{km}/3)^2 \end{bmatrix}. \tag{35}$$

Both the nominal and samples of the dispersed atmospheric density are provided by Mars-GRAM 2010. The nominal bank angle is set as a piecewise-linear function of velocity, with the nodes

$\cos^{-1}(\bar{u})$	70°	70°	45°	45°	10°	10°
$\bar{V}$	6 km/s	5.5 km/s	2.5 km/s	1.1 km/s	1 km/s	0 km/s

(36)

The resulting nominal entry trajectory is shown in Figure 5. Closed-loop range control is provided by the Apollo final phase guidance algorithm [1, 31], which is described in the following.

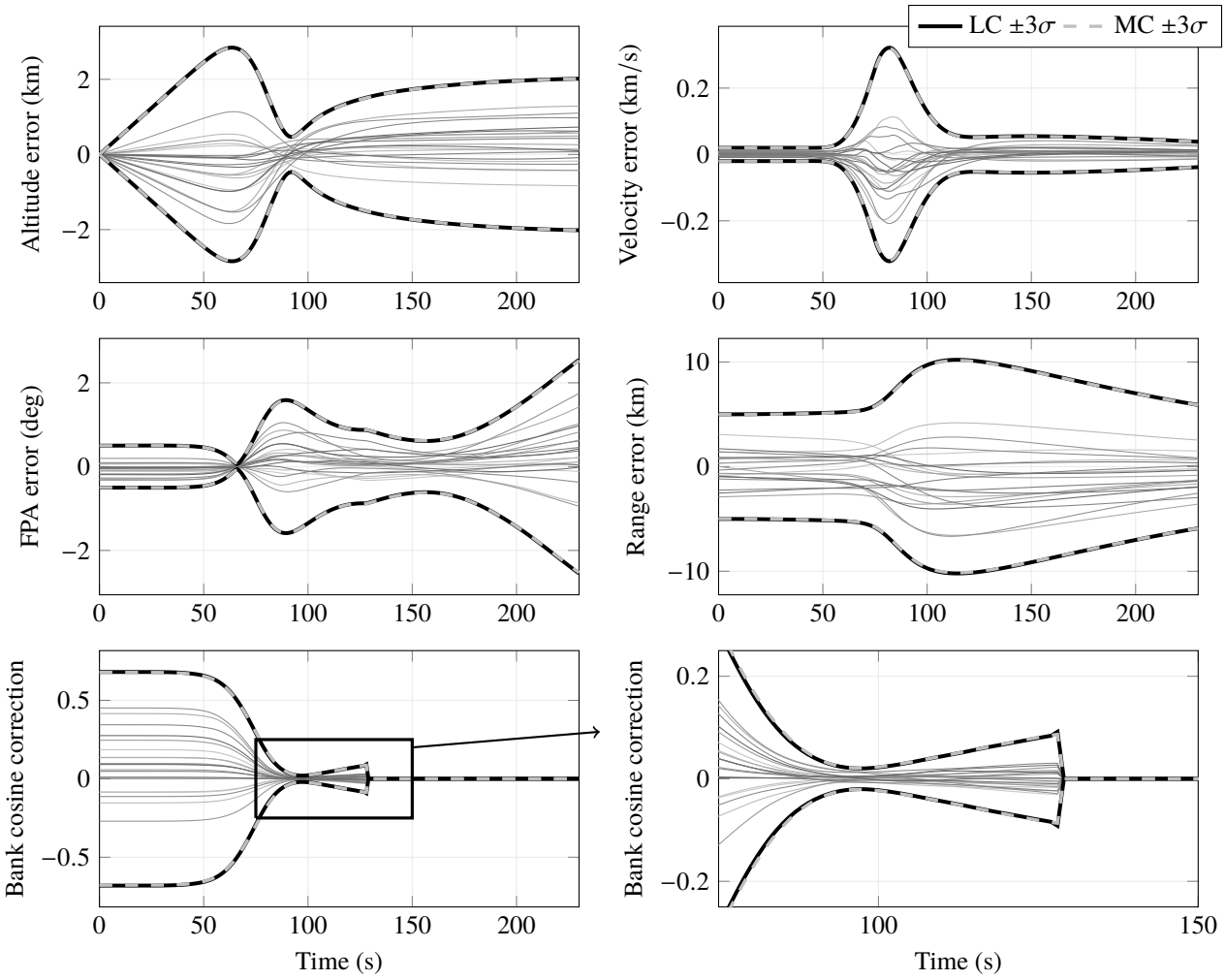

Fig. 6 Sample closed-loop entry trajectories with 3σ bounds computed from both 5,000 trial Monte Carlo (MC) and linear covariance (LC).

2. Apollo Final Phase Guidance

Let $f(t, x, u, p_0)$ be the right hand side of the equation (26), with control $u = \cos\sigma$, and define the system matrices

$$A(t) = \frac{\partial f}{\partial x}\big(\bar{x}(t), \bar{u}(t), 0\big), \qquad B(t) = \frac{\partial f}{\partial u}\big(\bar{x}(t), \bar{u}(t), 0\big), \tag{37}$$

evaluated along the nominal trajectory $\bar{x}(t)$, nominal control $\bar{u}(t)$, and with nominal density $\bar{\rho}(h)$ (i.e., $\bar{p}_0 = 0$). The adjoint state (λ, λ_u) to the system (26) is defined as the solution to the backwards ODE

$$\frac{\mathrm{d}}{\mathrm{d}t}\begin{bmatrix}\lambda(t)\\ \lambda_u(t)\end{bmatrix} = -\begin{bmatrix}A^{\mathsf{T}}(t) & 0\\ B^{\mathsf{T}}(t) & 0\end{bmatrix}\begin{bmatrix}\lambda(t)\\ \lambda_u(t)\end{bmatrix}, \qquad \begin{bmatrix}\lambda(t_f)\\ \lambda_u(t_f)\end{bmatrix} = \begin{bmatrix}\lambda_f\\ 0\end{bmatrix}, \tag{38}$$

where the boundary value λ_f is a user-defined vector determining the relative effects of the final states on the final range error. For the Apollo final phase algorithm, this boundary value is set to

$$\lambda_f = \begin{bmatrix}-\cot\bar{\gamma}(t_f) & 0 & 0 & 1\end{bmatrix}^{\mathsf{T}}, \tag{39}$$

and the state feedback gain is defined in terms of the adjoint values as

$$K(t) = -K_{\mathrm{oc}}\frac{\lambda^{\mathsf{T}}(t)}{\lambda_u(t)}, \tag{40}$$

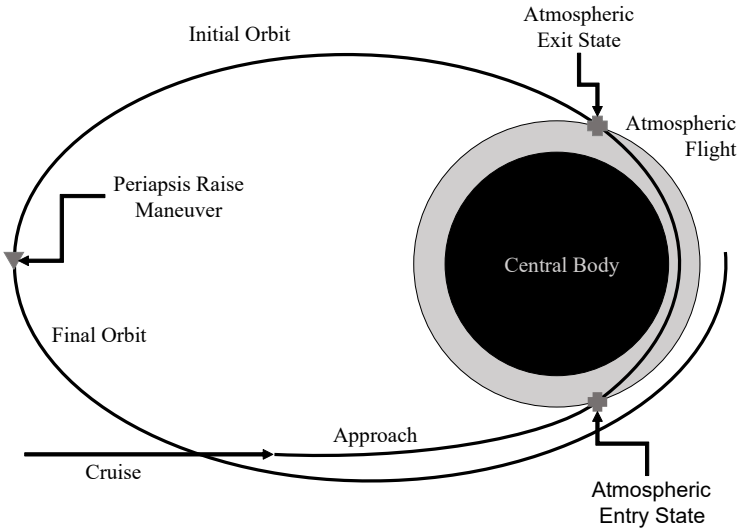

Fig. 7 Aerocapture sequence

where K_{oc} is a user-defined overcontrol gain. In this example, we set $K_{\text{oc}} = 4$. Furthermore, we assume that the (range) control effect is zero during the heading alignment phase, which begins when the vehicle velocity decreases below 1.1 km/s. Thus the control matrix is set to $B(t) = 0$ when $\bar{V}(t) \leq 1.1$ km/s.

The closed-loop bank angle cosine is thus given by the linear feedback law (33). In practice, the nominal control $\bar{u}$, feedback gain K, and reference trajectory $\bar{x}$ are all set as functions of velocity. But, for the purposes of linear covariance analysis, we assume these reference values are set as functions of time. The closed-loop, linearized system is thus described by the state matrix in (34).

3. Results

The closed-loop entry trajectory dispersions, due to both the initial state uncertainty and the MarsGRAM-generated density variations, are computed using two methods: Monte Carlo, for which 5,000 sample trajectories are integrated, each with a fixed MarsGRAM density profile sample; and by linear covariance (LC) analysis, using a $q = 50$ dimensional KL representation of the density profile. Sample Monte Carlo trajectories together with 3σ bounds as computed by both the Monte Carlo and from LC are shown in Figure 6. The 3σ bounds from LC approximation is almost exactly equal to the bounds computed from Monte Carlo.

B. Mars Aerocapture

The same MSL-like vehicle performs an aerocapture trajectory at Mars. Aerocapture is when a vehicle flies a single pass through a planet's atmosphere, reducing the energy of the spacecraft enough to capture into orbit. This atmospheric flight phase is followed by a propulsive periapsis raise maneuver with a nonzero nominal ΔV magnitude, and then additional maneuvers to adjust apoapsis and out of plane errors as necessary; see Figure 7. For this scenario, the desired final orbit is circular at $2,000$ km altitude.

For the aerocapture scenario the vehicle parameters, Mars properties, and atmospheric flight dynamics are all identical to the entry scenario. The nominal initial altitude, planet-relative velocity, and downrange distance are also identical to the entry case, with a shallower entry flight path angle of $-9.8°$. Smaller dispersions on the initial state are used for the aerocapture case, such that they are Gaussian distributed about the nominal values with 3σ errors of 10 m/s and $0.2°$ for velocity and flight path angle, respectively. Downrange distance is not particularly relevant to longitudinal aerocapture dynamics so is not dispersed, and initial altitude is again assumed to be exactly 125 km. Thus

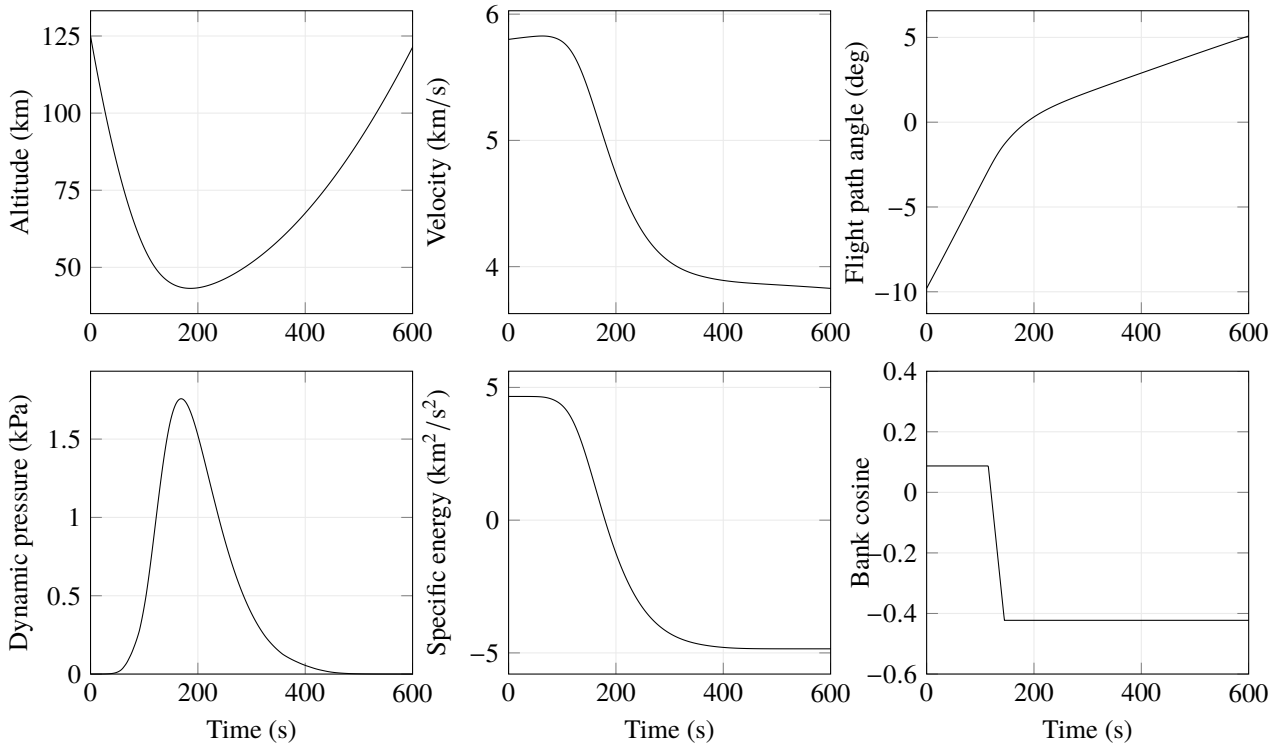

Fig. 8 Nominal areocapture trajectory

for aerocapture the initial state is Gaussian distributed as

$$x_0 \sim \mathcal{N}(\bar{x}_0, P_0), \quad \text{where} \quad \bar{x}_0 = \begin{bmatrix} 125\,\text{km} + r_p \\ 5.8\,\text{km/s} \\ -9.8^\circ \\ 0 \end{bmatrix}, \quad P_0 = \begin{bmatrix} 0 & & & \\ & (10\,\text{m/s}/3)^2 & & \\ & & (0.2^\circ/3)^2 & \\ & & & 0 \end{bmatrix}. \tag{41}$$

As a point of reference, MSL required entry flight path angle delivery within $3\sigma = 0.2^\circ$ and entry velocity knowledge of $3\sigma = 2.0$ m/s [32]. Mars-GRAM 2010 was again used for the nominal and dispersed atmospheric density profiles.

The nominal bank angle profile is assumed to have a bang-bang form with a single transition from lift-up to lift-down during the flight. To provide margin for feedback, the vehicle has an initial bank angle of $\sigma = 85^\circ$ from entry until some switching time t_s, then linearly increases the bank angle over a duration of 30 sec until reaching a final bank angle of $\sigma = 115^\circ$, and finally the bangle angle $\sigma = 115^\circ$ is held until atmospheric exit. The switching time t_s is solved by a foot-finding procedure so that the apoapsis after atmospheric exit equals a desired value. For this problem, the switching time was found to be $t_s = 114.9$ sec to meet a target apoapsis of $2,000$ km, and the resulting nominal trajectory is described by Figure 8.

In many ways aerocapture is the same as guided entry but with a different final objective, namely, targeting a Keplerian orbital state at atmospheric exit rather than a final range. Thus, we adapt the Apollo final phase guidance algorithm for aerocapture. This method of terminal point controller guidance for aerocapture is well-studied [33, 34]; the particular implementation used in this work is briefly reviewed here.

For this study, the closed-loop guidance during atmospheric flight is designed to target the desired apoapsis after atmospheric exit r_a, which is given as a function of the vehicle state $x_f = (r_f, V_f, \gamma_f, R_f)$ at atmospheric exit by

$$r_a = \frac{|\boldsymbol{h}_f|}{V_a}, \tag{42}$$

where $\boldsymbol{h}_f$ is the specific angular momentum and V_a is the velocity at apoapsis, which are given by

$$V_a = \frac{\mu_{\text{grav}} - \sqrt{\mu_{\text{grav}}^2 + 2\varepsilon_f |\boldsymbol{h}_f|^2}}{|\boldsymbol{h}_f|}, \qquad |\boldsymbol{h}_f| = r_f V_f \cos\gamma_f, \tag{43}$$

where,

$$\varepsilon_f = \frac{V_f^2}{2} - \frac{\mu_{\text{grav}}}{r_f} \tag{44}$$

is the specific energy. Note that in (42)-(44) the states are inertial, not planet-relative; when using the simplified longitudinal dynamics in (26), which assume a nonrotating spherical planet, the inertial and planet-relative states become identical.

After the atmosphere pass, two maneuvers are required to ensure the spacecraft reaches the desired final orbit. First, a periapsis raise maneuver is performed at first apoapsis along the velocity direction and with magnitude ΔV_1; this maneuver has some nonzero nominal value because initially the periapsis will be below the atmospheric interface altitude. Second, an apoapsis correction maneuver is performed at periapsis (at its new altitude) in either the posigrade (to raise apoaisis) or retrograde (to lower apoapsis) direction and with magnitude ΔV_2. Nominally $\Delta V_2 = 0$, but the value of ΔV_2 is uncertain as this maneuver corrects for any apoapsis error following the atmospheric pass. Lateral dynamics, guidance, and a plane correction maneuver are all neglected for the purpose of this study. The magnitudes of these maneuvers can be computed as shown, where in this study the target orbit is assumed to be circular at some radius r_c (the equations are readily modified to eliminate this assumption). The magnitudes of the velocity at apoapsis after the first maneuver V_1 and the velocity at periapsis before the second maneuver V_2 are given by

$$V_1 = \sqrt{\frac{2\mu_{\text{grav}} r_c}{r_a(r_a + r_c)}} \qquad V_2 = \sqrt{\frac{2\mu_{\text{grav}} r_a}{r_c(r_a + r_c)}}, \tag{45}$$

where V_c is the circular velocity at the radius r_c, given by

$$V_c = \sqrt{\frac{\mu_{\text{grav}}}{r_c}}. \tag{46}$$

Finally, the total maneuver cost ΔV is computed as the sum

$$\Delta V = \Delta V_1 + \Delta V_2 = (V_1 - V_a) + |V_c - V_2|. \tag{47}$$

Because of the absolute value sign in the expression for ΔV_2, the partial derivatives become undefined at the nominal value $\Delta V_2 = 0$. Therefore, in this work only ΔV_1 is linearly predicted.

The aerocapture guidance algorithm consists of integrating the same dynamics for the adjoint state (λ, λ_u) using the same open-loop system matrices $A(t)$ and $B(t)$ evaluated along the nominal aerocapture trajectory. The state feedback gain matrix $K(t)$ is also computed the same way and user-defined overcontrol gain is again used, this time with a value $K_{\text{oc}} = 3$. The first of two differences in the guidance is that the control is active until $t = 240$ sec, at which point the feedback control is set to zero, i.e. $B(t) = 0$ when $t > 240$ sec. This time was selected to correspond approximately to when the energy stops decreasing in the reference trajectory, and was set so that the Apollo guidance would remain well-behaved with minimal modifications.

The second difference between the aerocapture and entry guidance implementations is the way the boundary value λ_f is computed. Following the terminal control theory, the terminal condition is set equal to the partial derivative of a performance index $\Theta(t)$ with respect to the state, evaluated at the final time [35]. In Ref. [33], total ΔV is used as the performance index; in this study we use radius of apoapsis error, where the target apoapsis radius r_c falls out of the partial derivative given by

$$\lambda_f^{\mathsf{T}} = \frac{\delta\Theta(t_f)}{\delta x(t_f)} = \left(\frac{\delta r_a}{\delta x}\right)_{t=t_f}. \tag{48}$$

The construction of this control law implicitly assumes a constant bank angle [33] (even though the reference bank profile is not necessarily constant), and therefore apoapsis targeting is a nearly-equivalent proxy for ΔV optimization; a difference in the two solutions would only be expected for steep entry flight path angles [5]. The partial derivatives of apoapsis radius, apoapsis velocity, and total ΔV, each with respect to the state, are provided in the appendix. The aerocapture closed-loop guidance algorithm is implemented as in (37), (38), and (40)-(34), replacing the boundary value in (39) with the value for apoapsis targeting in (48).

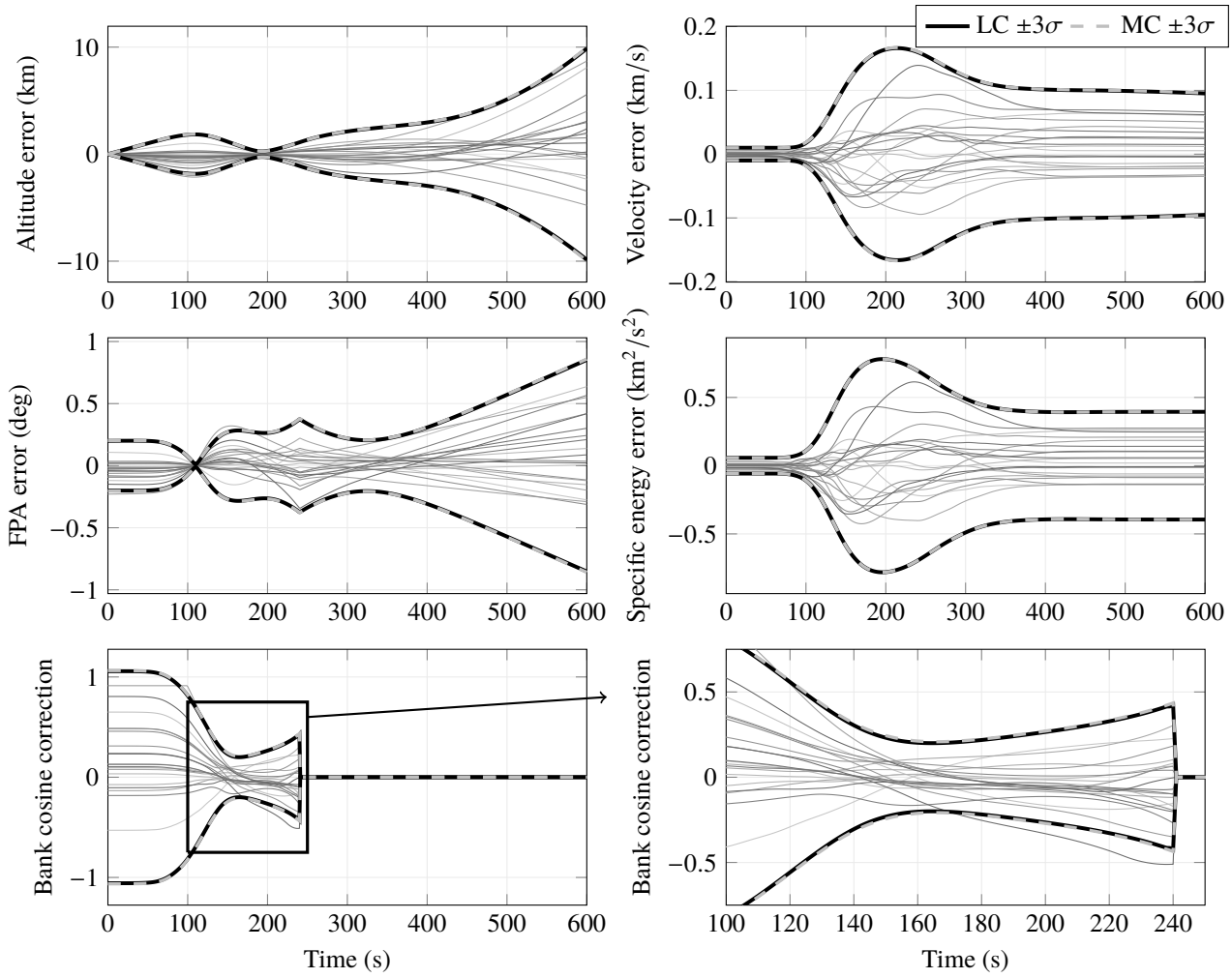

Fig. 9 Sample closed-loop aerocapture trajectories with 3σ bounds computed from both 5,000 trial Monte Carlo (MC) and linear covariance (LC).

1. Results

As with the guided entry example, dispersions are estimated using both a 5,000-trial Monte Carlo analysis and a linear covariance analysis using a $q = 50$ dimensional KL representation of density variability. The trajectory dispersions are compared in Figure 9. Additionally, histograms of the Monte Carlo results for apoapsis altitude, velocity at apoapsis, and total ΔV are shown in Figure 10 with a Gaussian-fit probability density function estimated from the linear covariance analysis superimposed.

C. Discussion

The numerical examples show a close match between the Monte Carlo estimates and linear covariance approximations, as seen by the plots of standard deviation over time in Figures 6 and 9. This suggests that the implemented control laws keep the dispersed trajectories close enough to the reference for the linearization to remain accurate, and the linear feedback nature of these control laws enables estimating the full closed-loop system. It also suggests that the KL expansion of density models the MarsGRAM density variability well enough to make accurate predictions of this dynamical system. The aerocapture numerical example demonstrates how these predictions can be translated into performance metrics, such as a histogram of apoapsis targeting or 99th-percentile value of total ΔV, ΔV_{99}.

The main purpose of these two numerical examples was to show that the Monte Carlo and linear covariance analysis predictions matched, and this has been achieved. A next step would be removing some of the simplifying assumptions

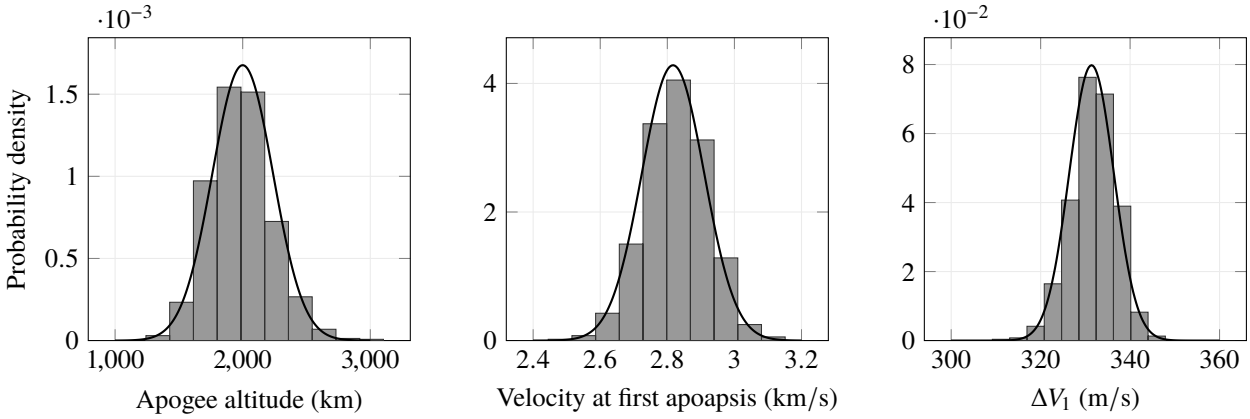

Fig. 10 Statistics of post-aerocapture orbit from both 5,000 trial Monte Carlo (histograms) and from the linear covariance (Gaussian fit).

regarding the dynamics and guidance algorithms to implement this linear prediction in a more realistic simulation. Planetary rotation and nonspherical gravity terms were neglected and, for aerocapture in particular, these can be important effects. Lateral dynamics and guidance were not accounted for, and though these are often handled somewhat independently using bank reversals, the finite time spent reversing bank introduces a coupling between longitudinal and lateral guidance that is not considered here. The reference trajectory could also be further optimized for both of these examples to improve targeting performance, and the overcontrol could vary over the reference trajectory as a function of time, velocity, or energy. For the aerocapture guidance, traditionally terminal point control implements the feedback table as a function of energy instead of time as performed here.

One avenue for potential future work is to incorporate such predictions into an onboard guidance scheme. For example, a numerical predictor-corrector could be wrapped around the linear feedback control, propagating the linear covariance and using ΔV_{99} as the error function instead of propagating single deterministic trajectories. The linear predictions could also be used to optimize the nominal trajectory and overcontrol value(s) to minimize ΔV_{99} with constraints on control saturation. Overcontrol could become a function of time and apply differently to different state errors as part of this process.

V. Conclusion

This paper considered the problem of applying linear covariance analysis to systems for which the primary source of uncertainty is spatially, rather than temporally, defined. Gaussian random fields were used to represent the spatial uncertainty, and the Karhunen–Loève decomposition was used to parameterize the field-dependent uncertainty. The efficacy of the proposed method was demonstrated for closed-loop hypersonic flight during both entry and aerocapture.

In future work, the developed theory could be applied to chance-constrained optimization of closed-loop systems in Gaussian random fields. On another future direction, linear covariance analysis could be used to supplement on-board trajectory optimization, or could enable an uncertainty analysis in early trade studies.

Appendix

A. Partial Derivatives

The following partial derivatives are assumed to be evaluated along a nominal trajectory as a function of time, but explicit dependence on time is suppressed for notational simplicity.

1. Common Terms

The equations of motion (26) are rewritten below in the form $\dot{x} = f(t, x, u(t,x), p_0) = (f_r, f_V, f_\gamma, f_R)$ as

$$\dot{r} = f_r = V \sin\gamma, \tag{49a}$$

$$\dot{V} = f_V = -\frac{\rho V^2}{2\beta} - \frac{\mu_{\text{grav}} \sin\gamma}{r^2}, \tag{49b}$$

$$\dot{\gamma} = f_\gamma = \frac{\rho V E}{2\beta}\cos\sigma - \left(\frac{\mu_{\text{grav}}}{r^2} - \frac{V^2}{r}\right)\frac{\cos\gamma}{V}, \tag{49c}$$

$$\dot{R} = f_R = V\cos\gamma. \tag{49d}$$

Each component of the A matrix, defined by (7), is given below for atmospheric flight. Note that these sensitivities make use of the atmospheric density scale height H defined such that $\partial\rho/\partial h = -\rho/H$, but this is not equivalent to assuming an exponential atmosphere, and H can be numerically estimated at each altitude for any density profile. Thus:

$$\frac{\partial f_r}{\partial r} = 0, \quad \frac{\partial f_r}{\partial V} = \sin\gamma, \quad \frac{\partial f_r}{\partial \gamma} = V\cos\gamma, \quad \frac{\partial f_r}{\partial R} = 0, \tag{50}$$

$$\frac{\partial f_V}{\partial r} = \frac{\rho V^2}{2H\beta} + \frac{2\mu_{\text{grav}}\sin\gamma}{r^3}, \quad \frac{\partial f_V}{\partial V} = -\frac{\rho V}{\beta}, \quad \frac{\partial f_V}{\partial V} = -\frac{\rho V}{\beta}, \quad \frac{\partial f_V}{\partial R} = 0, \tag{51}$$

$$\frac{\partial f_\gamma}{\partial r} = -\frac{\rho V E}{2H\beta}\cos\sigma + \left(\frac{2\mu_{\text{grav}}}{r^3} - \frac{V^2}{r^2}\right)\frac{\cos\gamma}{V}, \quad \frac{\partial f_\gamma}{\partial V} = \frac{\rho E}{2\beta}\cos\sigma + \frac{\cos\gamma}{r}\left(\frac{\mu_{\text{grav}}}{V^2 r} + 1\right), \tag{52a}$$

$$\frac{\partial f_\gamma}{\partial \gamma} = \left(\frac{\mu_{\text{grav}}}{r^2} - \frac{V^2}{r}\right)\frac{\sin\gamma}{V}, \quad \frac{\partial f_\gamma}{\partial R} = 0, \tag{52b}$$

$$\frac{\partial f_R}{\partial r} = 0, \quad \frac{\partial f_R}{\partial V} = \cos\gamma, \quad \frac{\partial f_R}{\partial \gamma} = -V\sin\gamma, \quad \frac{\partial f_R}{\partial R} = 0. \tag{53}$$

Each component of the B matrix, defined by Eq. 37, is given below for atmospheric flight where the control is $u = \cos\sigma$:

$$\frac{\partial f_r}{\partial u} = 0, \quad \frac{\partial f_V}{\partial u} = 0, \quad \frac{\partial f_\gamma}{\partial u} = \frac{\rho V E}{2\beta}, \quad \frac{\partial f_R}{\partial u} = 0. \tag{54}$$

The C matrix is computed based on the terms in the KL expansion of density variability, following (24) and (25) where the GRF in this case is density $\rho(z)$. The partial derivatives of the dynamics with respect to density are given by (55), and the partial derivatives of density with respect to the uncertain parameters p_0 are given by (56) below

$$\frac{\partial f_r(t)}{\partial \rho(h)} = 0, \qquad \frac{\partial f_V(t)}{\partial \rho(h)} = -\frac{V^2}{2\beta}, \qquad \frac{\partial f_\gamma(t)}{\partial \rho(h)} = \frac{VEu}{2\beta}, \qquad \frac{\partial f_R(t)}{\partial \rho(h)} = 0, \tag{55}$$

$$\frac{\partial \rho(h)}{\partial p_0} = \begin{bmatrix} \frac{\partial \rho(h)}{\partial w_1} & \cdots & \frac{\partial \rho(h)}{\partial w_q} \end{bmatrix}, \quad \text{where} \quad \frac{\partial \rho(h)}{\partial w_i} = \sqrt{\lambda_i}\phi_i(h). \tag{56}$$

As per (7), the ith row of the C matrix is then built by multiplying $\partial f_i(t)/\partial\rho(h)$ (a scalar) by $\partial\rho(h)/\partial p_0$ (a $1 \times q$ matrix), then prepending n zeros to the row, such that the dimensions of C are $n \times (n+q)$.

2. Aerocapture

The aerocapture guidance law uses the partial derivative of apoapsis radius at the final state (at or after atmospheric exit) to compute the adjoint state terminal condition. Partial derivatives of the apoapsis velocity and ΔV_1 with respect to the final state are also used during analysis. The states in the following equations must be *inertial*, meaning either a nonrotating planet is assumed or the full state is converted from planet-relative to inertial before these expressions are evaluated.

Begin by noting that downrange distance has no impact on any of these derivatives.

$$\frac{\partial r_a}{\partial R_f} = 0, \quad \frac{\partial V_a}{\partial R_f} = 0, \quad \frac{\partial \Delta V_1}{\partial R_f} = 0. \tag{57}$$

Next, note that the circular (final) orbit velocity is not impacted by the final states and so this term drops out of the ΔV partial derivative:

$$\frac{\partial V_c}{\partial r_f} = 0, \quad \frac{\partial V_c}{\partial V_f} = 0, \quad \frac{\partial V_c}{\partial \gamma_f} = 0. \tag{58}$$

Now write the partial derivatives of energy and magnitude of angular momentum with respect to the states,

$$\frac{\partial \varepsilon_f}{\partial r_f} = \frac{\mu_{\text{grav}}}{r_f^2}, \quad \frac{\partial \varepsilon_f}{\partial V_f} = V_f, \quad \frac{\partial \varepsilon_f}{\partial \gamma_f} = 0, \tag{59}$$

$$\frac{\partial |\boldsymbol{h}_f|}{\partial r_f} = V_f \cos\gamma_f, \quad \frac{\partial |\boldsymbol{h}_f|}{\partial V_f} = r_f \cos\gamma_f, \quad \frac{\partial |\boldsymbol{h}_f|}{\partial \gamma_f} = -r_f V_f \sin\gamma_f. \tag{60}$$

The states affect the velocity at apoapsis through the energy and the magnitude of angular momentum, so take its partial derivatives with respect to these quantities.

$$\frac{\partial V_a}{\partial |\boldsymbol{h}_f|} = -\left(\frac{V_a}{|\boldsymbol{h}_f|} + \frac{2\varepsilon_f}{\sqrt{\mu_{\text{grav}}^2 + 2\varepsilon_f |\boldsymbol{h}_f|^2}} \right), \quad \frac{\partial V_a}{\partial \varepsilon_f} = -\frac{|\boldsymbol{h}_f|}{\sqrt{\mu_{\text{grav}}^2 + 2\varepsilon_f |\boldsymbol{h}_f|^2}}. \tag{61}$$

The partial derivatives of velocity at apoapsis with respect to the states can then be found via chain rule using the partial derivatives we've already computed.

$$\frac{\partial V_a}{\partial r_f} = \frac{\partial V_a}{\partial |\boldsymbol{h}_f|}\frac{\partial |\boldsymbol{h}_f|}{\partial r_f} + \frac{\partial V_a}{\partial \varepsilon_f}\frac{\partial \varepsilon_f}{\partial r_f}, \quad \frac{\partial V_a}{\partial V_f} = \frac{\partial V_a}{\partial |\boldsymbol{h}_f|}\frac{\partial |\boldsymbol{h}_f|}{\partial V_f} + \frac{\partial V_a}{\partial \varepsilon_f}\frac{\partial \varepsilon_f}{\partial V_f}, \quad \frac{\partial V_a}{\partial \gamma_f} = \frac{\partial V_a}{\partial |\boldsymbol{h}_f|}\frac{\partial |\boldsymbol{h}_f|}{\partial \gamma_f} + \frac{\partial V_a}{\partial \varepsilon_f}\frac{\partial \varepsilon_f}{\partial \gamma_f}. \tag{62}$$

Now make use of those derivatives in a similar chain rule expression for the derivatives of apoapsis radius, where the derivatives of r_a with respect to $|\boldsymbol{h}_f|$ and V_a were included directly in the expressions below.

$$\frac{\partial r_a}{\partial r_f} = \frac{1}{V_a}\frac{\partial |\boldsymbol{h}_f|}{\partial r_f} - \frac{|\boldsymbol{h}_f|}{V_a^2}\frac{\partial V_a}{\partial r_f}, \quad \frac{\partial r_a}{\partial V_f} = \frac{1}{V_a}\frac{\partial |\boldsymbol{h}_f|}{\partial V_f} - \frac{|\boldsymbol{h}_f|}{V_a^2}\frac{\partial V_a}{\partial V_f}, \quad \frac{\partial r_a}{\partial \gamma_f} = \frac{1}{V_a}\frac{\partial |\boldsymbol{h}_f|}{\partial \gamma_f} - \frac{|\boldsymbol{h}_f|}{V_a^2}\frac{\partial V_a}{\partial \gamma_f}. \tag{63}$$

The states affect the velocity at apoapsis after maneuver 1, V_1, only through the apoapsis radius r_a, so we take that derivative below.

$$\frac{\partial V_1}{\partial r_a} = -\frac{\mu_{\text{grav}} r_c (2r_a + r_c)}{V_1 r_a^2 (r_a + r_c)^2} \tag{64}$$

Now use chain rule to find the derivatives of V_1 with respect to the states.

$$\frac{\partial V_1}{\partial r_f} = \frac{\partial V_1}{\partial r_a}\frac{\partial r_a}{\partial r_f}, \quad \frac{\partial V_1}{\partial V_f} = \frac{\partial V_1}{\partial r_a}\frac{\partial r_a}{\partial V_f}, \quad \frac{\partial V_1}{\partial \gamma_f} = \frac{\partial V_1}{\partial r_a}\frac{\partial r_a}{\partial \gamma_f}, \tag{65}$$

Finally, combine the velocity partial derivatives to get the partial derivatives of ΔV_1 with respect to the states.

$$\frac{\partial \Delta V_1}{\partial r_f} = \frac{\partial V_1}{\partial r_f} - \frac{\partial V_a}{\partial r_f}, \quad \frac{\partial \Delta V_1}{\partial V_f} = \frac{\partial V_1}{\partial V_f} - \frac{\partial V_a}{\partial V_f}, \quad \frac{\partial \Delta V_1}{\partial \gamma_f} = \frac{\partial V_1}{\partial \gamma_f} - \frac{\partial V_a}{\partial \gamma_f}. \tag{66}$$

Acknowledgments

This work was supported by NASA Space Technology Research Fellowships 80NSSC17K0093 and 80NSSC19K1139. S. W. Albert thanks Eric Queen and Alireza Doostan for their assistance with TPC guidance and KL expansions, respectively.

References

[1] Moseley, P. E., "The Apollo Entry Guidance: A Review of the Mathematical Development and its Operational Characteristics," TRW Note No. 69-FMT-791, December 1969.

[2] Mendeck, G. F., and Craig McGrew, L., "Entry Guidance Design and Postflight Performance for 2011 Mars Science Laboratory Mission," *Journal of Spacecraft and Rockets*, Vol. 51, No. 4, 2014, pp. 1094–1105. doi:10.2514/1.A32737.

[3] Putnam, Z. R., Neave, M. D., and Barton, G. H., "PredGuid entry guidance for Orion return from low Earth orbit," *2010 IEEE Aerospace Conference*, Big Sky, MT, 2010, pp. 1–13. doi:10.1109/AERO.2010.5447010.

[4] Lu, P., "Entry Guidance: A Unified Method," *Journal of Guidance, Control, and Dynamics*, Vol. 37, No. 3, 2014, pp. 713–728. doi:10.2514/1.62605.

[5] Lu, P., Cerimele, C. J., Tigges, M. A., and Matz, D. A., "Optimal Aerocapture Guidance," *Journal of Guidance, Control, and Dynamics*, Vol. 38, No. 4, 2015, pp. 553–565. doi:10.2514/1.G000713.

[6] Woffinden, D., Robinson, S., Williams, J., and Putnam, Z. R., "Linear Covariance Analysis Techniques to Generate Navigation and Sensor Requirements for the Safe and Precise Landing Integrated Capabilities Evolution (SPLICE) Project," *AIAA Scitech Forum*, San Diego, CA, 2019, p. 0662. doi:10.2514/6.2019-0662.

[7] Ridderhof, J., and Tsiotras, P., "Planetary Entry in a Randomly Perturbed Atmosphere," *AIAA Guidance, Navigation, and Control Conference*, Virtual event, 2021. doi:10.2514/6.2021-1218.

[8] Ridderhof, J., Tsiotras, P., and Johnson, B., "Stochastic Entry Guidance," , 2021. URL `https://arxiv.org/abs/2103.05168`.

[9] Alabau-Boussouira, F., Brockett, R., Glass, O., Le Rousseau, J., and Zuazua, E., *Control of Partial Differential Equations*, Lecture Notes in Mathematics, Vol. 2048, Springer, Cetraro, Italy, 2012. doi:10.1007/978-3-642-27893-8.

[10] Chen, Y., Georgiou, T. T., and Pavon, M., "Optimal Steering of a Linear Stochastic System to a Final Probability Distribution, Part I," *IEEE Transactions on Automatic Control*, Vol. 61, No. 5, 2016, pp. 1158–1169. doi:10.1109/TAC.2015.2457784.

[11] Ridderhof, J., Okamoto, K., and Tsiotras, P., "Nonlinear Uncertainty Control with Iterative Covariance Steering," *IEEE 58th Conference on Decision and Control*, Nice, France, 2019, pp. 3484–3490. doi:10.1109/CDC40024.2019.9029993.

[12] Okamoto, K., Goldshtein, M., and Tsiotras, P., "Optimal Covariance Control for Stochastic Systems Under Chance Constraints," *IEEE Control Systems Letters*, Vol. 2, No. 2, 2018, pp. 266–271. doi:10.1109/LCSYS.2018.2826038.

[13] Ridderhof, J., and Tsiotras, P., "Minimum-Fuel Closed-Loop Powered Descent Guidance with Stochastically Derived Throttle Margins," *Journal of Guidance, Control, and Dynamics*, Vol. 44, No. 3, 2021, pp. 537–547. doi:10.2514/1.G005400.

[14] Spencer, D. A., and Braun, R. D., "Mars Pathfinder atmospheric entry - Trajectory design and dispersion analysis," *Journal of Spacecraft and Rockets*, Vol. 33, No. 5, 1996, pp. 670–676. doi:10.2514/3.26819.

[15] Desai, P. N., Mitcheltree, R. A., and Cheatwood, F. M., "Entry Dispersion Analysis for the Stardust Comet Sample Return Capsule," *Journal of Spacecraft and Rockets*, Vol. 36, No. 3, 1999, pp. 463–469. doi:10.2514/2.3467.

[16] Jiang, X., "Uncertainty Quantification for Mars Atmospheric Entry using Polynomial Chaos and Spectral Decomposition," *2018 AIAA Guidance, Navigation, and Control Conference*, Kissimmee, FL, 2018. doi:10.2514/6.2018-1317.

[17] Halder, A., and Bhattacharya, R., "Dispersion Analysis in Hypersonic Flight During Planetary Entry Using Stochastic Liouville Equation," *Journal of Guidance, Control, and Dynamics*, Vol. 34, No. 2, 2011, pp. 459–474. doi:10.2514/1.51196.

[18] Heidrich, C. R., and Braun, R. D., "Aerocapture Trajectory Design in Uncertain Entry Environments," *AIAA Scitech 2020 Forum*, Orlando, FL, 2020. doi:10.2514/6.2020-1741.

[19] Ridderhof, J., and Tsiotras, P., "Chance-Constrained Covariance Steering in a Gaussian Random Field via Successive Convex Programming," 2021. URL `https://arxiv.org/abs/2101.09634`.

[20] Albert, S. W., Doostan, A., and Schaub, H., "Finite-Dimensional Density Representation for Aerocapture Uncertainty Quantification," *AIAA Scitech 2021 Forum*, Virtual event, 2021. doi:10.2514/6.2021-0932.

[21] Khalil, H., *Nonlinear Systems*, Prentice Hall, 2002, Chap. 3, pp. 99–103.

[22] Markley, F. L., and Carpenter, J. R., "Generalized Linear Covariance Analysis," *The Journal of Astronautical Sciences*, Vol. 57, 2009.

[23] Le Gall, J.-F., *Brownian Motion, Martingales, and Stochastic Calculus*, Graduate Texts in Mathematics, Springer International Publishing, 2016. doi:10.1007/978-3-319-31089-3.

[24] Rasmussen, C. E., and Williams, C. K. I., *Gaussian Processes for Machine Learning*, Adaptive Computation and Machine Learning, The MIT Press, 2005. doi:10.7551/mitpress/3206.001.0001.

[25] Kosambi, D. D., "Statistics in Function Space," *Journal of the Indian Mathematical Society*, Vol. 7, 1943, pp. 76–88.

[26] Naylor, A. W., and Sell, G. R., *Linear Operator Theory in Engineering and Science*, Applied Mathematical Sciences, Vol. 40, Springer-Verlag, 1982.

[27] Betz, W., Papaioannou, I., and Straub, D., "Numerical Methods for the Discretization of Random Fields by Means of the Karhunen–Loève Expansion," *Computer Methods in Applied Mechanics and Engineering*, Vol. 271, 2014, pp. 109–129. doi:10.1016/j.cma.2013.12.010.

[28] Sudret, B., and Der Kiureghian, A., "Stochastic Finite Element Methods and Reliability: A State-of-the-Art Report," Tech. Rep. UCB/SEMM-2000/08, Department of Civil and Environmental Engineering, University of California Berkley, 2000.

[29] Vinh, N. X., Busemann, A., and Culp, R. D., *Hypersonic and Planetary Entry Flight Mechanics*, The University of Michigan Press, 1980, Chap. 2, pp. 26–27.

[30] Justh, H., Justus, C., and Ramey, H., "Mars-GRAM 2010: improving the precision of Mars-GRAM," *4th International Workshop on the Mars Atmosphere: Modelling and Observations*, Paris, France, 2011, pp. 1–4.

[31] Carman, G. L., Ives, D. G., and Geller, D. K., "Apollo-Derived Precision Lander Guidance," *23rd Atmospheric Flight Mechanics Conference*, Boston, MA, 1998. doi:10.2514/6.1998-4570.

[32] Martin-Mur, T. J., Kruizinga, G. L., Burkhart, P. D., Abilleira, F., Wong, M. C., and Kangas, J. A., "Mars Science Laboratory Interplanetary Navigation," *Journal of Spacecraft and Rockets*, Vol. 51, No. 4, 2014, pp. 1014–1028. doi:10.2514/1.A32631.

[33] Ro, T., and Queen, E., "Study of Martian aerocapture terminal point guidance," *23rd Atmospheric Flight Mechanics Conference*, Boston, MA, 1998. doi:10.2514/6.1998-4571.

[34] Rousseau, S., Perot, E., Graves, C., Masciarelli, J., and Queen, E., "Aerocapture Guidance Algorithm Comparison Campaign," *AIAA/AAS Astrodynamics Specialist Conference and Exhibit*, Monterey, CA, 2002. doi:10.2514/6.2002-4822.

[35] Bryson, A. E., and Ho, Y.-C., *Applied Optimal Control: Optimization, Estimation and Control*, Ginn and Company, 1975, Chap. 2, p. 48. doi:10.1201/9781315137667.